
Article:
Henning, R., Sturm, P., Geddes, D.A. et al. (3 more authors) (2022) The influence of curing temperature on the strength and phase assemblage of hybrid cements based on GGBFS/FA blends. Frontiers in Materials, 9. 982568. ISSN 2296-8016

https://doi.org/10.3389/fmats.2022.982568

---

frontiers | Frontiers in Materials

TYPE Original Research
PUBLISHED 20 September 2022
DOI 10.3389/fmats.2022.982568

OPEN ACCESS

EDITED BY
Neven Ukrainczyk,
Darmstadt University of Technology, Germany

REVIEWED BY
Sanjay Kumar,
National Metallurgical Laboratory (CSIR), India
Pengkun Hou,
University of Jinan, China

*CORRESPONDENCE
Gregor J. G. Gluth,
gregor.gluth@bam.de

SPECIALTY SECTION
This article was submitted to Structural Materials,
a section of the journal
Frontiers in Materials

RECEIVED 30 June 2022
ACCEPTED 08 August 2022
PUBLISHED 20 September 2022

CITATION
Henning R, Sturm P, Geddes DA, Keßler S, Walkley B and Gluth GJ (2022), The influence of curing temperature on the strength and phase assemblage of hybrid cements based on GGBFS/FA blends.
Front. Mater. 9:982568.
doi: 10.3389/fmats.2022.982568

The influence of curing temperature on the strength and phase assemblage of hybrid cements based on GGBFS/FA blends

Ricky Henning [1], Patrick Sturm [1], Daniel A. Geddes[2,3], Sylvia Keßler [4], Brant Walkley [3] and Gregor J. G. Gluth [1]*

[1]Division 7.4 Technology of Construction Materials, Bundesanstalt für Materialforschung und -prüfung (BAM), Berlin, Germany, [2]Department of Materials Science and Engineering, The University of Sheffield, Sheffield, United Kingdom, [3]Department of Chemical and Biological Engineering, The University of Sheffield, Sheffield, United Kingdom, [4]Engineering Materials and Building Preservation, Helmut-Schmidt-University/University of the Federal Armed Forces Hamburg, Hamburg, Germany

Hybrid cements are composites made of Portland cement or Portland clinker and one or more supplementary cementitious materials like slag, fly ash or metakaolin, activated with an alkali salt. To date, their hydration mechanism and the phase formation at various temperatures is insufficiently understood, partly due to the large variability of the raw materials used. In the present study, three hybrid cements based on ground granulated blast furnace slag, fly ash, Portland clinker and sodium sulfate, and an alkali-activated slag/fly ash blend were cured at 10 and 21.5°C, and subsequently analyzed by XRD, ^{27}Al MAS NMR, and TGA. The compressive strength of the hybrid cements was higher by up to 27% after 91-day curing at 10°C, compared to curing at 21.5°C. The experimental results as well as thermodynamic modeling indicate that the differences in compressive strength were related to a different phase assemblage, mainly differing amounts of strätlingite and C-N-A-S-H, and the associated differences of the volume of hydration products. While the strätlingite was amorphous to X-rays, it could be identified by ^{27}Al MAS NMR spectroscopy, TGA and thermodynamic modeling. The microstructural properties of the hybrid cements and the alkali-activated slag/fly ash blend as well as the compatibility between thermodynamic modeling results and experimental data as a function of curing temperature and time are discussed.

KEYWORDS

hybrid cement, curing, compressive strength, ground granulated blast furnace slag, fly ash, strätlingite

1 Introduction

Cements based on low amounts of ordinary Portland cement (OPC) or Portland clinker and high fractions of supplementary cementitious materials (SCMs), activated with an alkali salt, are often called hybrid cements. Their chemical composition is intermediate between those of OPC and alkali-activated materials (AAMs) (Shi et al., 2011). The purpose of the activator is to increase the rate of dissolution of the SCMs to accelerate the formation of calcium sodium aluminium silicate hydrate (abbreviated as C-N-A-S-H in cement notation) and other cementitious phases and, thus, setting and hardening of the cement (Garcia-Lodeiro et al., 2016). The main hydration product of hybrid cements is C-N-A-S-H, a compound related to calcium silicate hydrate (C-S-H) present in OPC, formed by substitution of silicon with aluminium in the tetrahedral bridging sites of the silica chains and associated uptake of alkali ions to balance the negative charge arising from Al^{3+} in 4-fold coordination (Garcia-Lodeiro et al., 2016). As a result of the reduced amount of OPC and the high fraction of SCMs, hybrid cements usually exhibit significantly less heat of hydration than plain OPC, while maintaining sufficient high early compressive strength (Lee et al., 2003; Garcia-Lodeiro et al., 2013; Garcia-Lodeiro et al., 2016; Alahrache et al., 2017; Donatello et al., 2018; Mota et al., 2019; Fu et al., 2021; Gluth and Garel, 2021; Xue et al., 2021). In addition, there are chemical and mineralogical similarities between hybrid cements and the cements of ancient Roman concretes that have survived in a marine, *i.e.*, strongly corrosive, saline, environment for several centuries (Jackson et al., 2013; Jackson et al., 2014; Jackson et al., 2018; Palomo et al., 2019), implying an excellent durability of concretes based on hybrid cements in salt-rich environments such as seawater (Palomo et al., 2019).

However, due to the variety of the applied activators and SCMs, the hydration process and phase assemblage of hybrid cements differ in various studies, and they are not fully understood to date. For example, the chemical compositions of ground granulated blast furnace slags (GGBFS) differ significantly between materials from different sources, especially regarding the amount of available silicon, alumina and magnesia, which influence the formation of hydration products of alkali-activated slags (Ben Haha et al., 2012; Bernal et al., 2014). As for hybrid cements, materials with fly ash as the sole SCM (Lee et al., 2003; Garcia-Lodeiro et al., 2013; Garcia-Lodeiro et al., 2016; Alahrache et al., 2017; Donatello et al., 2018) as well as materials with GGBFS as the sole SCM (Angulo-Ramírez et al., 2017; Mota et al., 2019; Fu et al., 2021; Gluth and Garel, 2021; Xue et al., 2021) have been studied in considerable detail. In contrast, studies of hybrid cements based on blends of GGBFS and fly ash (Gluth and Garel, 2021; Xue et al., 2021) are scarce, although a large amount of work on AAMs indicates that blending GGBFS with other SCMs can yield advantageous behavior and properties of the resulting materials, and previous experience shows that employment of such blends is a way to control the heat release and the setting times of hybrid cements (Gluth and Garel, 2021; Xue et al., 2021). Thus, it is desirable and necessary to understand the behavior of hybrid cements based on GGBFS/fly ash blends in more detail than is hitherto available.

A number of studies show that the hydration of OPC and blends with SCMs are sensitive to the curing temperature; *viz.* curing temperatures around 50–60°C greatly promote the early hydration of OPC and alkali-activated materials, leading to higher early compressive strength (Escalante-Garcia and Sharp, 1998; Escalante-Garcia, 2003; Lothenbach et al., 2007; Lothenbach et al., 2008; Sun and Vollpracht, 2018; Hu et al., 2020), but decrease the late strengths. The accelerated hydration of clinker phases, mainly alite, leads to heterogeneous formation of hydration products around the clinker particles and ultimately to a coarser porosity, which manifests in a lower compressive strength. At lower curing temperature a more homogeneous distribution of hydration products together with a lower porosity occurs in OPC, and thus a higher compressive strength is observed (Lothenbach et al., 2007). Additional factors that influence the compressive strength are the changes of morphology of C-S-H or C-N-A-S-H and the formation of additional hydration products, the amount of ettringite and the formation of different AFm phases (Matschei et al., 2007a; Matschei et al., 2007b; Lothenbach et al., 2008; Bahafid et al., 2017).

While several studies have investigated conventional cements (OPC and OPC-SCM blends) in this regard, the influence of the curing temperature on the phase assemblage and strength of hybrid cements has not yet been studied in detail. This issue is of general relevance, as concrete placement and curing often takes place at temperatures below standard laboratory temperatures. Moreover, the influence of curing temperature is particularly important in applications where hybrid cements are used below-ground at low temperatures. Examples are sealing structures in underground waste storage facilities, for which hybrid cements appear to particularly adequate, due to their low heat of hydration.

To investigate the influence of curing temperature on the properties of hardened hybrid cements based on GGBFS/fly ash blends, four cements were produced in the present study from varying fractions of Portland clinker (Pc; 0–14 wt%), ground granulated blast furnace slag (GGBFS; 32–38 wt%), fly ash (FA; 49–58 wt%), and sodium sulfate (2–4 wt%) as activator. The resulting cement pastes were cured at 10 and 21.5°C, for durations of 28 and 91 days. Compressive strength testing, X-ray diffraction (XRD) measurements, thermogravimetric analysis, ^{27}Al magic-angle spinning nuclear magnetic resonance (MAS NMR) spectroscopy and thermodynamic modeling were performed to analyze the phase assemblages and deduce their influence on the properties of the hardened cements.

TABLE 1 Chemical compositions[a] (in wt%) of the starting materials.

Oxide/LOI	CaO	SiO_2	Al_2O_3	Fe_2O_3	MgO	Na_2O	K_2O	SO_3	LOI[b]
Pc	62.9	23.3	5.6	2.5	1.3	0.3	0.8	1.7	0.7
GGBFS	46.1	36.9	8.1	0.4	6.5	0.4	0.4	0.6	1.2
FA	7.6	53.0	23.3	7.9	2.3	1.1	1.1	0.9	2.0

[a]Determined by inductively coupled plasma optical emission spectroscopy (ICP-OES) after total microwave digestion.
[b]Loss on ignition at 1000°C according to DIN EN, 196-2.

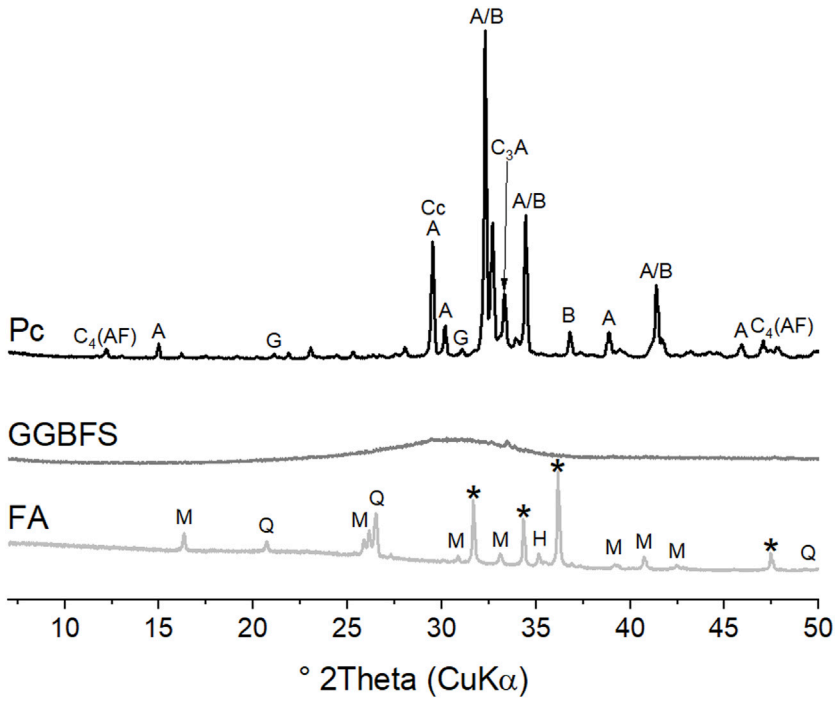

FIGURE 1
XRD patterns of the starting materials. Major reflections are labelled C_4AF, ferrite; A, alite; B, belite; C_3A, tricalcium aluminate; G, gypsum; Cc, calcite; M, mullite; Q, quartz; H, hematite, *, zincite (internal standard).

2 Materials

2.1 Starting materials

The hybrid cements were prepared with a Portland clinker CEM I 42.5 R (Pc), obtained from a cement manufacturer. The Pc granules were ground for 18 s in a disk mill, and the powder was sieved (mesh width = 0.90 mm); grains exceeding the mesh width were ground for further 18 s and sieved again. GGBFS and a hard coal FA were the used as SCMs. The chemical compositions of the starting materials, determined by ICP-OES after total microwave digestion, are shown in Table 1. The employed sodium sulfate (Na_2SO_4) was of analytical grade.

The X-ray diffraction (XRD) patterns of the starting materials are shown in Figure 1. The amounts of the phases present in Pc and FA were obtained by Rietveld quantitative phase analysis (RQPA); the results are shown in Table 2 (for measurement conditions Section 3.2). The GGBFS was almost completely amorphous, indicating a highly reactive state, but a small quantity of merwinite was identified through a minor reflection at 33.3° 2θ.

The densities of the Pc, the GGBFS, the FA and the sodium sulfate were 3.17, 2.92, 2.37 and 2.66 cm^3/g, respectively. The median particle sizes (d_{50}) of the Pc, the GGBFS and the FA were 15.5, 13.0 and 10.2 µm, respectively. The particle size distributions of the starting materials, determined by laser granulometry after dispersion in isopropanol, are shown in

TABLE 2 Phase assemblages (in wt%) of the starting materials Pc and FA.

Phase	Pc	FA
Alite	65.0	-
Belite	16.3	-
C_3A	10.1	-
C_4AF	5.5	-
Calcite	2.4	-
Gypsum	0.4	-
Mullite	-	26.9
Quartz	-	9.1
Hematite	-	5.5
Anhydrite	-	1.4
Amorphous	-	56.2

Supplementary Figure S1 in the Electronic Supplementary Material.

2.2 Sample preparation

Cements were designed by varying the amount of Pc between 0 and 14.4 wt%, and the activator dosage in the range 2–4 wt%, at a constant GGBFS/FA mass ratio of 1:1.5. The activator (sodium sulfate) dosage range was specified based on previous studies, which indicate that this range yields optimum performance (Donatello et al., 2018; Mota et al., 2019; Fu et al., 2021; Gluth and Garel, 2021). All cements were mixed with deionized water at a water/cement (*w*/*c*) ratio of 0.35 by mass to obtain workable pastes (*c* comprises all solid components, including the sodium sulfate). The mix designs are presented in Table 3. The samples are designated C*x*S*y* according to the contents of Portland clinker (C) and sodium sulfate (S) in the dry cement, with *x* and *y* representing the respective fractions in the formulations. Since C0S4 contained no Pc, it is not a hybrid cement in the strict sense; it is more appropriately referred to as alkali-activated GGBFS/FA blend.

Mixing of the cement pastes was done in a planetary centrifugal mixer at a rotation speed of 1250 rpm for 240 s. Subsequently, the pastes were filled into silicon molds with dimensions of 20 mm × 20 mm × 20 mm, which were sealed with polyvinylchloride film and stored at 10°C or 21.5°C until measured. The cubic specimens were removed from the molds and used to measure the compressive strength after 28 and 91 days of curing. Fracture pieces obtained by strength testing were used for the microstructural analyses.

3 Methods

3.1 Compressive strength testing

Compressive strength testing was conducted using a ToniPRAX device in accordance with DIN EN-196-1:2019 but with only one 10th loading rate (240 N/s) to allow for the dimensions of the specimens (20 mm × 20 mm × 20 mm). For all cement samples, the average compressive strength from three replicates is presented below with the respective standard deviation.

3.2 X-ray diffraction

Prior to the XRD measurements, the hydration of the hybrid cements was stopped after 28 and 91 days of curing. To this end, fracture pieces were crushed manually, and subsequently 50 ml of isopropanol were added. Exchange of isopropanol was done after 3 h, 1 day, and 3 days. After a total duration of 7 days, the pieces were rinsed (on type 1025 filter paper) using additional isopropanol. Thereafter, the samples were dried at 40°C for 24 h. Subsequently, a fine powder for XRD measurements was obtained by grinding in a McCrone 'micronizing' mill. 3 g of the dry pieces were dispersed in 10 ml isopropanol and ground for 3.5 min at medium speed. The resulting slurries were dried at 40°C overnight. The obtained powders were filled into the XRD sample holders by side loading to minimize preferred orientation effects.

Powders of the unhydrated starting materials (Pc, GGBFS and FA) were obtained by manually grinding the materials with mortar and pestle. The powders were filled into the sample holders by side loading to minimize preferred orientation effects.

TABLE 3 Mix designs of the cement pastes.

	Pc (wt%)	GGBFS (wt%)	Fly ash (wt%)	Na_2SO_4 (wt%)	*w*/*c*
C0S4	-	38.4	57.6	4.0	0.35
C5S4	4.8	36.5	54.7	4.0	0.35
C5S2	4.9	37.2	55.9	2.0	0.35
C14S4	14.4	32.6	49.0	4.0	0.35

XRD measurements were performed on a Rigaku Ultima IV device using Cu Kα radiation (λ = 1.5419 Å) in Bragg-Brentano geometry. The parameters for the XRD measurements were set to: cathode at 40 kV/40 mA, 1/6°/10 mm divergence slit, scanning range 7–95°2θ, sampling interval 0.01°2θ and scanning speed 0.2°2θ/min.

Rietveld qualitative phase analysis (RQPA) of the Pc and the FA was done by using TOPAS-Academic v.5. LaB_6 (NIST Standard Reference Material 660c) was used to determine the device parameters. Zincite (10 wt%) was added to FA before grinding, but not to the Pc [an amorphous fraction of ~0% was assumed (Snellings et al., 2014), *i.e.*, RQPA performed without internal standard]. Additional measurements on the zincite were performed to refine its structure under the applied measurement conditions; the obtained zincite structure file was used in the RQPA. The crystallography information files, containing the crystal structures for refinement, were taken from the ICSD and COD databases (Supplementary Table S1). Variations of the lattice parameters were allowed to max. 0.05 nm to keep the refinement stable. All peaks were fitted with fundamental parameter functions.

3.3 Thermogravimetric analysis

As for the XRD analyses (Section 3.2), the hydration was stopped in isopropanol, and fracture pieces of the samples were dried at 40°C. Fine powders of the samples were produced by manually grinding with mortar and pestle (agate). The preparation was done as gentle as possible; however, slight alterations of the hydrated phase assemblage (e.g., dehydration) cannot be excluded.

Thermogravimetric analyses were performed with a Netzsch STA 449 C Jupiter device. Sample masses of 10 mg were used for the TGA, which was conducted under flowing nitrogen gas at a heating rate of 10 K min^{-1}, starting at 40°C.

3.4 Nuclear magnetic resonance spectroscopy

Portions of the sample powders prepared for the XRD analyses (Section 3.2) were used for the ^{27}Al MAS NMR spectroscopy measurements.

Solid state single pulse ^{27}Al MAS NMR experiments were carried out on a Bruker Avance III HD 500 spectrometer at 11.7 T, yielding a Larmor frequency of 130.32 MHz, using a 4.0 mm dual resonance CP/MAS probe at a spinning speed of 12.5 kHz. The spectra were acquired using a 1.7 µs selective (π/6) excitation pulse, a relaxation delay of 10 s and a total of 256 scans. Chemical shifts were referenced to 1.0 M aqueous $Al(NO_3)_3$ at 0 ppm.

3.5 Thermodynamic modeling

Thermodynamic modeling was carried out using the Gibbs Energy Minimization Software (GEMS) (Wagner et al., 2012; Kulik et al., 2013) with the Cemdata18 database (Lothenbach et al., 2019) and the Nagra/PSI thermodynamic database.

Since the alkaline activator, sodium sulfate, forms sodium hydroxide in solution (Donatello et al., 2018), the simulation of the activity coefficients was done with the extended Debye-Hückel equation for NaOH-dominated solutions (Helgeson et al., 1981; Myers et al., 2015):

$$\log \gamma_i = \frac{-A_\gamma \cdot z_j^2 \cdot \sqrt{I}}{1 + \dot{a} B_\gamma \cdot \sqrt{I}} + b_\gamma I + \log \frac{x_{jw}}{X_w}. \quad (1)$$

$$I = \frac{1}{2} \sum_j c_j \cdot z_j^2. \quad (2)$$

where I (mol kg^{-1}) is the ionic strength of the solution, z_j is the charge and c_j the concentration of ion j in solution, and summation of their product is done over all ions in solution. A_γ ($kg^{0.5}$ $mol^{-0.5}$) and B_γ ($kg^{0.5}$ $mol^{-0.5}$ cm^{-1}) are temperature- and pressure-dependent electrostatic parameters, x_{jw} (mol) is the molar quantity of water, and X_w (mol) is the total amount of aqueous phase. The average ionic size is denoted by $\dot{a}$ (Å), while the parameter b_γ (kg mol^{-1}) accounts for the common short-range interactions of the charged species. For NaOH-dominated solutions, $\dot{a}$ is 3.31 Å, and b_γ is 0.098 kg mol^{-1}. All simulations, unless stated differently, were done with exclusion of gaseous components.

The bulk composition, represented by the relative amounts of oxides available to form the hydration products of the hybrid cements, is given by the composition of each starting material, their fractions in the hybrid cements, and the degree of hydration of each starting material. The total amount of each implemented oxide (O_X) is

$$O_X = \sum_i D_i \cdot F_i \cdot o_i. \quad (3)$$

with O_X being the relative amount of oxide in the paste, o_i the fraction of oxide in the starting material i, D_i the degree of hydration (DoH) of starting material i, and F_i the fraction of the starting material i in the paste.

While the chemical compositions and the fractions of each starting material are known for the cements (Tables 1, 3), the degree of hydration for each starting material had to be estimated. The degree of hydration of Pc used in the present study can be estimated by the equations proposed by Parrot and Killoh (1984) for neat OPC with the modifications by Lothenbach et al. (2008), or the equations by Taylor (1987) for blends of OPC and fly ash. The latter yield a DoH of 81% for Pc after 28 days if a blend of 48% Pc and 52% FA is assumed, while the former yield a DoH of 66% at the same curing duration. Both estimates are in reasonable agreement with experiments (Mota et al., 2019) for hybrid cements, composed of 30% white

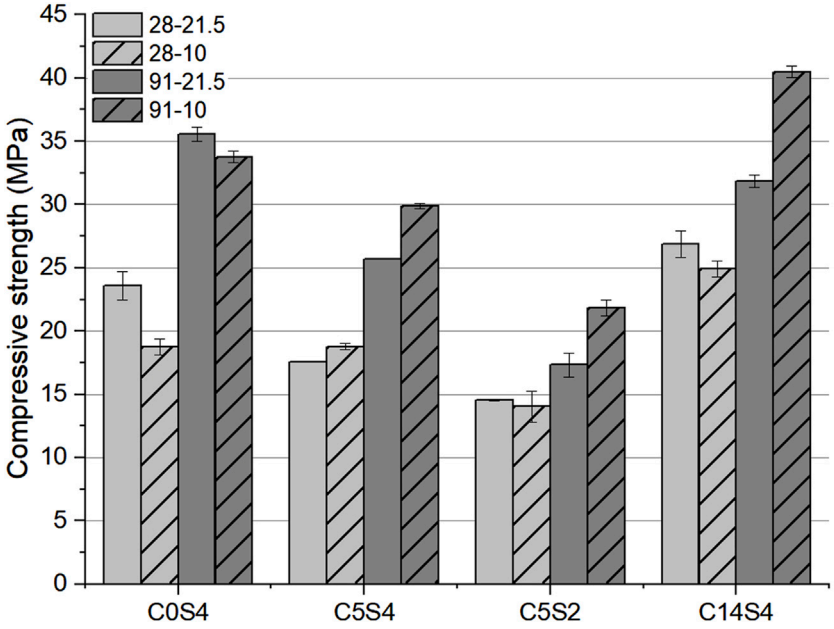

FIGURE 2
Compressive strength of the hybrid cements after 28 and 91 days of curing at 10 and 21.5°C. The designations in the legend denote curing duration and curing temperature.

Portland cement and 70% GGBFS, activated with Na_2SO_4. In these experiments, the DoH of the Portland cement was determined to be (70 ± 3) % after 28 days of curing. For the present simulations, a DoH of 70% for Pc in the hybrid cements was used. The DoH of the GGBFS was assumed to be 60%, following earlier estimates (Myers et al., 2015; Myers et al., 2017). According to experimental findings of De Weerdt et al. (2011), the DoH of the fly ash was assumed to be 20%. To simplify the complex chemistry of hybrid cements, the used thermodynamic model is based on a congruent dissolution of the raw materials.

The thermodynamic model for C-N-A-S-H was chosen to be the CNASH_ss model (Myers et al., 2014), designed for sodium- and aluminium-substituted C-S-H in AAMs and hybrid cements. The potential formation of N-A-S-H was considered by including zeolite X [$Na_2(Al_2Si_{2.5})O_9(H_2O)_2$] as an allowed phase in the modeling, because of its similar chemical composition and solubility (Gomez-Zamorano et al., 2017; Lothenbach et al., 2019; Walkley et al., 2020). The formation of gibbsite, goethite and hematite was excluded in the modeling because of kinetic restrictions (Lothenbach et al., 2019). Modeling included varying the hydration temperature in the range 5–100°C. All modeling results will be presented as phase assemblages referred to 100 g of hybrid cement (dry weight) with a *w*/*c* of 0.35.

Additional modeling was done in the presence of 500 g atmospheric air (equivalent to 0.075 g of CO_2/g of cement) to simulate the formation of calcite (carbonation). As a check of the robustness of the results, modeling was also performed in which the DoHs of the Pc, the GGBFS and the fly ash, respectively, were varied by ± 10% from the DoHs assumed for the above modeling.

4 Results and discussion

4.1 Compressive strength

The compressive strengths of the hybrid cements cured for 28 and 91 days at 10 and 21.5°C are summarized in Figure 2. The standard deviations of the results were generally low, indicating a high reproducibility of the compressive strengths. After 28 days of curing, three of the cements achieved a higher strength for curing at 21.5°C temperature. The difference in compressive strength was most pronounced for C0S4: 23.6 MPa at 21.5°C *versus* 18.8 MPa at 10°C. Only C5S4 achieved a higher compressive strength at 10°C (18.8 MPa), compared to curing at ambient temperature (17.6 MPa).

With extended hydration time an opposite relation between hydration temperature and compressive strength can be identified, *i.e.*, after 91 days a higher compressive strength is observed for a curing temperature of 10°C for three of the cements, namely the hybrid cements C5S4, C5S2, and C14S4. Compared to 21.5°C-curing, their compressive strength was higher by 27% (C14S4), 17% (C5S4) and 26% (C5S2) for curing at 10°C, with a maximum strength of 40.5 MPa for C14S4. The cement without Pc (C0S4)

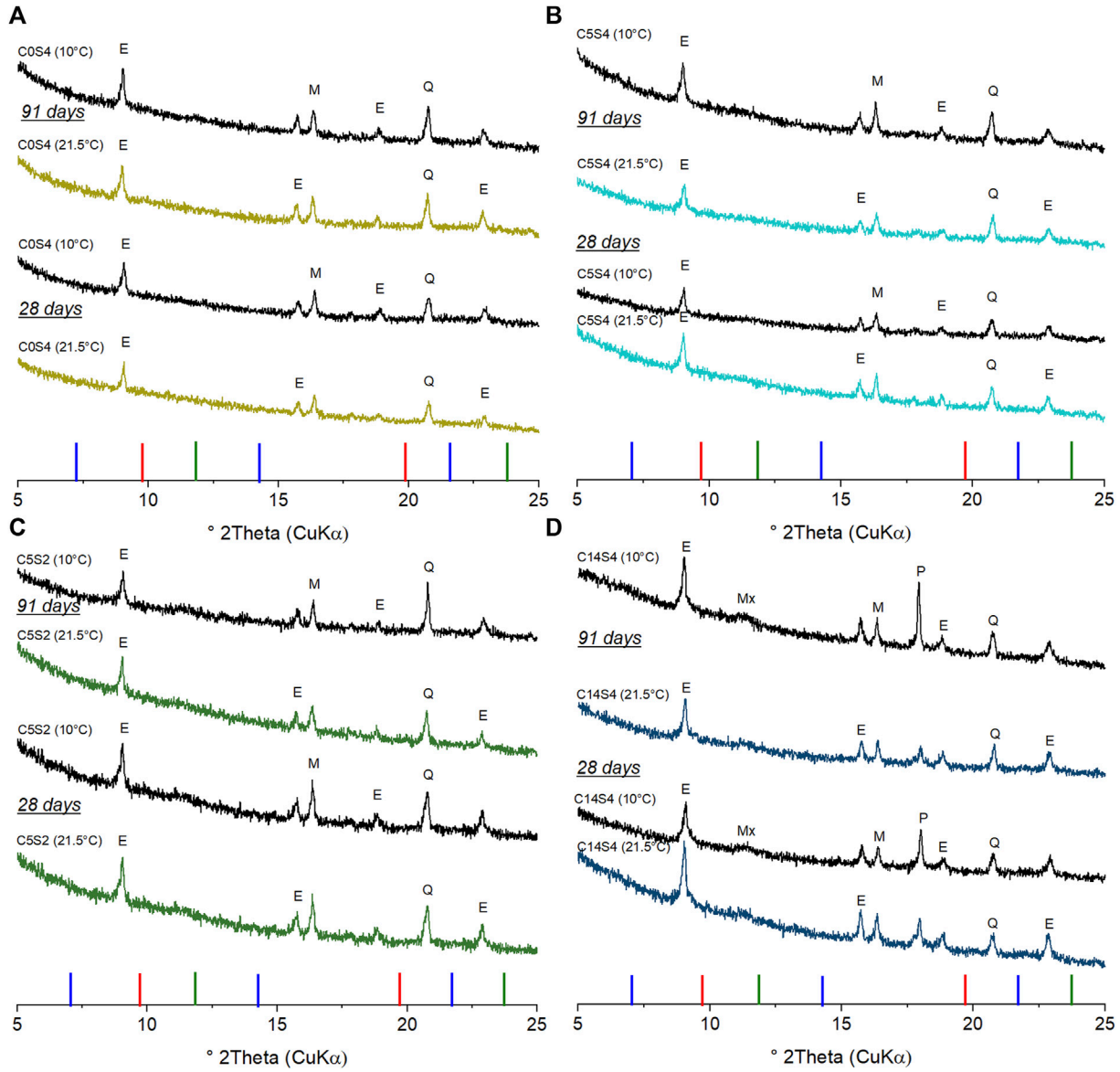

FIGURE 3
XRD patterns of the hybrid cements C0S4 **(A)**, C5S4 **(B)**, C5S2 **(C)**, C14S4 **(D)** after 28 and 91 days of curing at 10 and 21.5°C. Major reflections are labelled: E, ettringite; Mx, meixnerite (Mg-Al LDH); M, mullite; P, portlandite; Q, quartz. Reflections of strätlingite (blue), monocarboaluminate (green) and monosulfoaluminate (red) are presented as stick patterns below the diffractograms.

achieved a higher compressive strength (35.6 MPa) after 91 days of curing at 21.5°C than for curing at 10°C, but the difference between the two compressive strengths was small (~6%); moreover, the difference in compressive strength for C0S4 at the two different curing temperatures decreased with increasing hydration time.

In summary, while the alkali-activated GGFS/FA blend C0S4 exhibited the highest compressive strength for a curing temperature of 21.5°C at both curing times, the compressive strength of the hybrid cements C5S4, C5S2 and C14S4 tended to be higher for curing at 21.5°C after 28 days, but where always higher for curing at 10°C after 91 days.

4.2 Microstructural analyses

4.2.1 X-ray diffraction analysis

XRD analysis confirmed the presence of C-N-A-S-H as well as calcite in all four cements at all curing temperatures and curing durations (Supplementary Figures S2–S5). C-N-A-S-H was

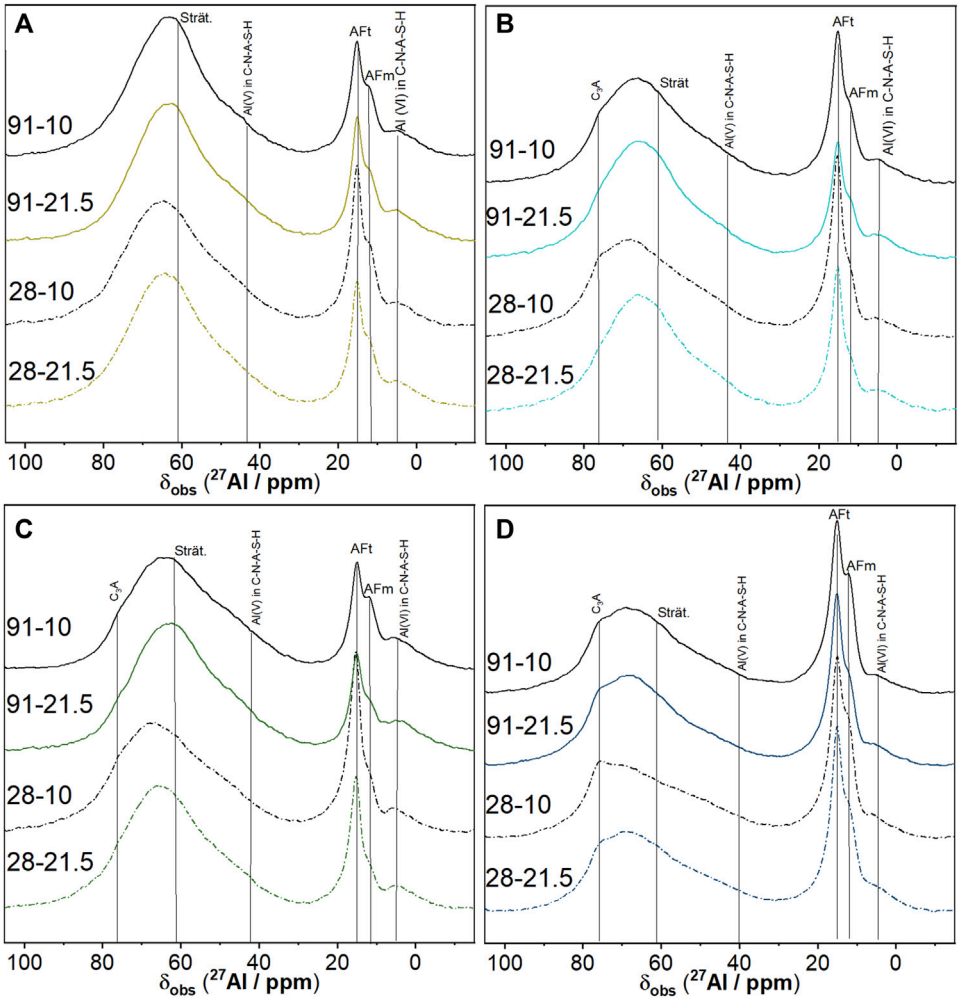

FIGURE 4
^{27}Al MAS NMR spectra of the hybrid cements C0S4 **(A)**, C5S4 **(B)**, C5S2 **(C)**, C14S4 **(D)** after 28 and 91 days of curing at 10 and 21.5°C. The designations of the spectra denote curing duration and curing temperature.

identified through the reflections of C-S-H (PDF# 00-034-0002). Its main reflection at approximately 29.4°2θ overlapped with a reflection of calcite (PDF# 00-005-0586), formed due to imperfect sealing of the samples during curing.

Figure 3 shows the XRD patterns in the range 5–25°2θ to focus on the diagnostic reflections of hydration products other than C-N-A-S-H. Ettringite (PDF# 00-041-1451) was formed in all hybrid cements, indicated by its main reflection at 9.1° 2θ. The stability of ettringite is favored by the high amounts of fly ash and sodium sulfate (Taylor et al., 2001; Lothenbach et al., 2011; Gluth and Garel, 2021), as the high sulfate content suppresses the formation of monosulfoaluminate. In contrast to the other hybrid cements, C14S4 contained portlandite (PDF# 00-044-1481) and small amounts of a meixnerite-type phase (Mg-Al layered double hydroxide, LDH; PDF# 00-038-0478). The main reflection of the meixnerite-type phase was broad, indicating that the phase was poorly crystalline. Portlandite is formed during the hydration of alite and belite, and it is consumed by GGBFS and FA to form C-S-H (or C-N-A-S-H in the present systems) *via* the pozzolanic reaction; accordingly, it could only be identified in hybrid cements with a sufficiently high amount of Pc (Alahrache et al., 2017). The reduction of the curing temperature to 10°C resulted in an increased intensity of the portlandite peak, which will be discussed below. In addition to these phases, mullite (PDF# 00-015-0776) and quartz (PDF# 00-046-1045), both unreactive impurities in the FA (*cf.* Figure 1 and Table 2), were identified in the diffractograms of all cements. No indications of crystalline AFm phases were found in the diffractograms.

4.2.2 Nuclear magnetic resonance spectroscopy

Figure 4 shows the ^{27}Al MAS NMR spectra of the hybrid cements after 28 and 91 days of curing at 10 and 21.5°C. The

spectra contain resonance signals in the ranges of tetrahedrally coordinated Al (50–80 ppm), pentahedrally coordinated Al (20–50 ppm), and octahedrally coordinated Al (−5–20 ppm) (Walkley and Provis, 2019).

The broad signal located around 55–80 ppm arises due to resonances in both 4-coordinated Al in the glassy phase of unreacted FA and GGBFS (Ben Haha et al., 2012; Bernal et al., 2013; Burciaga-Diaz and Escalante-Garcia, 2013; Myers et al., 2013; Murgier et al., 2014; Gardner et al., 2015), and 4-coordinated Al substituting for Si in the silicate chains of the C-N-A-S-H (Andersen et al., 2004; Sun et al., 2006; Bach et al., 2012; Walkley and Provis, 2019; Joseph et al., 2020). However, as these signals overlap within the same chemical shift region of the present spectra, they cannot be identified separately unambiguously. Nevertheless, resonances of 5-coordinated and 6-coordinated Al at approximately 40 ppm and 4–5 ppm, respectively, usually associated with C-A-S-H and assigned to the "third aluminate hydrate" (TAH) (Sun et al., 2006; Renaudin et al., 2009; Myers et al., 2015) or hydrated Al in the silicate chains (Kunhi Mohammed et al., 2020), are identified in the spectra of the cement pastes, confirming the formation of C-N-A-S-H. 4- and 6-coordinated Al in mullite is characterized by resonances at 45–50 ppm and 0 to −5 ppm, respectively (Sanz et al., 1984; He et al., 2004); however, these resonances cannot be identified unambiguously in the spectra, due to the low content of mullite in the hybrid cements.

A shoulder around 76 ppm is visible in the spectra of the hybrid cements C5S4, C5S2 and C14S4, but not in the spectra of C0S4. This signal is most prominent after 28 days of curing at 10°C for each of the three hybrid cements; furthermore, the signal is more intense in the spectrum of C14S4, compared to C5S2 and C5S4, *i.e.*, its intensity increased with increasing Pc fraction. The signal can thus be assigned to remaining C_3A, whose hydration is strongly delayed at high concentrations of sulfate ions (Joseph et al., 2020).

Besides the resonance of 6-coordinated Al in C-N-A-S-H, the region −5 to 20 ppm contains the signals of 6-coordinated Al in AFt and AFm phases. A strong signal at approximately 15 ppm and a partly overlapping peak or shoulder at 11.8–12 ppm are present in the spectra of all cement pastes (Figure 4). The signal at 15 ppm is attributed to ettringite, while the signal at approximately 12 ppm is generally related to AFm phases and/or Mg-Al LDH (hydrotalcite- or meixnerite-type phases) in hydrated cements (Skibsted et al., 1993; Jones et al., 2003; Myers et al., 2015; Walkley and Provis, 2019). The presence of ettringite in the cement pastes was shown by the XRD analyses; however, unequivocal evidence of AFm phases was not found in the XRD patterns (Figure 3). Poorly crystalline meixnerite was detected only in C14S4; nevertheless, the signal at 11.8–12 ppm was present in the ^{27}Al MAS NMR spectra of all cement pastes. Notably, the intensity of this signal was highest for long curing times (91 days) and a low curing temperature (10°C) for the hybrid cement pastes C5S4, C5S2 and C14S4, while its intensity appeared to be less dependent on curing time and temperature for C0S4, which contained no Pc (Figure 4). It can thus be concluded that the signal is caused by an AFm or LDH phase that formed preferentially at low curing temperature and advanced age in the hybrid cements that contain Pc; this phase is likely strätlingite, as will be discussed below. If strätlingite was present, a signal of its 4-coordinated Al at 61 ppm could be expected in the ^{27}Al MAS NMR spectra (Kwan et al., 1995; Sun et al., 2006; Dai et al., 2014; Frias and Martinez-Ramirez 2014). As with the resonances of 4-coordinated Al in the silicate chains of the C-N-A-S-H, discussed above, this signal can, however, not be identified separately in the present spectra because of the overlapping strong resonances of the unreacted FA and GGBFS.

4.2.3 Thermogravimetric analysis

The TGA/DTG curves of the pastes after 28 and 91 days of curing at 10 and 21.5°C are shown in Figure 5. The hybrid cement C14S4 showed the highest total weight loss (1000°C) for all curing durations and temperatures, which is likely due to this cement forming the highest amount of hydration products, caused by the high amount of Pc. For each of the four cements, there were differences between the total mass losses obtained for pastes cured under different conditions (duration and temperature); however, these were mainly related to the mass losses in the range 50–90°C, which are due to the decomposition of ettringite, C-N-A-S-H and possibly magnesium silicate hydrate gel (M-S-H) (Lothenbach et al., 2016; Bernard et al., 2019). As these phases are particularly prone to drying damage during sample grinding, these differences may not reflect actual differences between the phase abundances; consequently, the following analysis will focus on DTG peaks at higher temperatures.

A shoulder can be seen in the DTG curves of all cement pastes around 140°C, and a less intensive peak was observed in the temperature range 320–370°C. Based on published DTG curves (Matschei et al., 2007a; Matschei et al., 2007b; Lothenbach et al., 2012; Gluth et al., 2014; Lothenbach et al., 2016), these signals can be assigned to the decomposition of AFm phases (e.g. monocarboaluminate, monosulfoaluminate, strätlingite) or hydrotalcite- or meixnerite-type LDH phases. Additionally, the peak at 320–370°C could also be related to the decomposition of $Al(OH)_3$. However, while a meixnerite-type phase was observed in C14S4 (Figure 3.), none of these phases were observed in the XRD patterns of the other cement pastes. Thus, it can be concluded that some amorphous or poorly crystalline AFm phase (s) and/or $Al(OH)_3$ had precipitated in the cements. It can further be noted that there was a trend of a higher intensity of the corresponding peak at 320–370°C for the hybrid cement pastes cured at 10°C, compared to the pastes cured at 21.5°C.

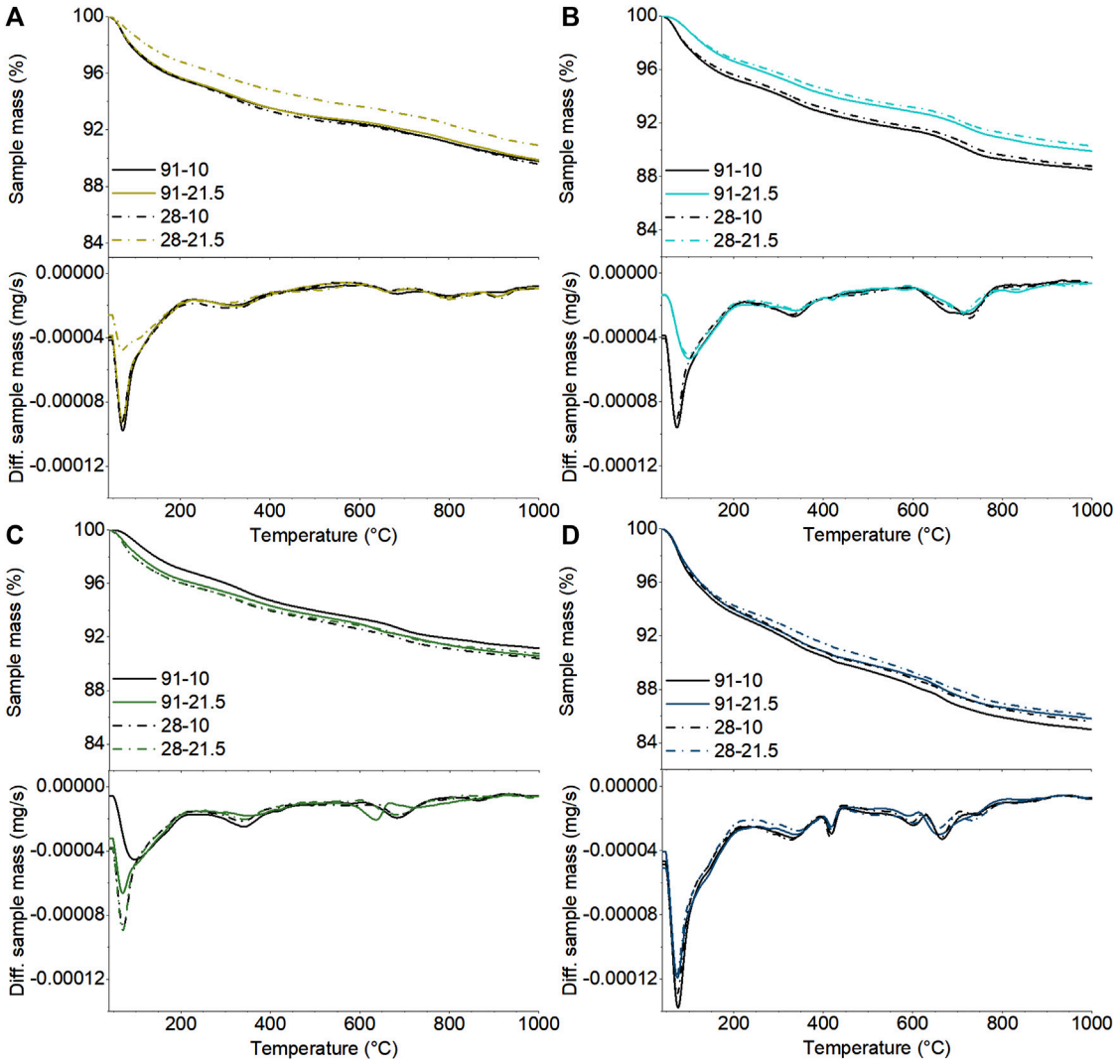

FIGURE 5
TGA and DTG curves of the cement pastes C0S4 **(A)**, C5S4 **(B)**, C5S2 **(C)** and C14S4 **(D)** after 28 and 91 days of curing at 10 and 21.5°C. The designations in the legends denote curing duration and curing temperature.

The hybrid cement with the highest Pc content, C14S4, exhibited an additional signal at 410–430°C, which is assigned to the decomposition of portlandite (Lothenbach et al., 2016), in line with the XRD results (Figure 3.). However, the higher amount of portlandite for the pastes cured at 10°C, determined by XRD, was not fully reflected in the TGA/DTG results, which may be due to sampling effects, e.g., different degrees of carbonation of the samples used for XRD and TGA/DTG, respectively.

The mass losses at temperatures above ~570°C are due the decomposition of $CaCO_3$ (Thiery et al., 2007; Lothenbach et al., 2016), which were incorporated in the pastes as calcite from the anhydrous Pc, and which could form in addition during carbonation of the samples. It can be noted that the TGA/DTG curves of C14S4 exhibited three peaks in the relevant temperature range, indicating that different polymorphs of $CaCO_3$ were present (Thiery et al., 2007), while only calcite was detected by XRD.

Two additional signals can be identified for C0S4 in the temperature range of 790–900°C. These are assigned to the decomposition of sodium sulfate (Wiedemann and Smykatz-Kloss 1981; Eysel et al., 1985) that had remained in the paste or formed during drying. Notably, the absence or very low intensity of these signals in the other hybrid cements indicates that the sodium sulfate had virtually completely reacted to ettringite, likely related to the higher availability of CaO in these latter cements.

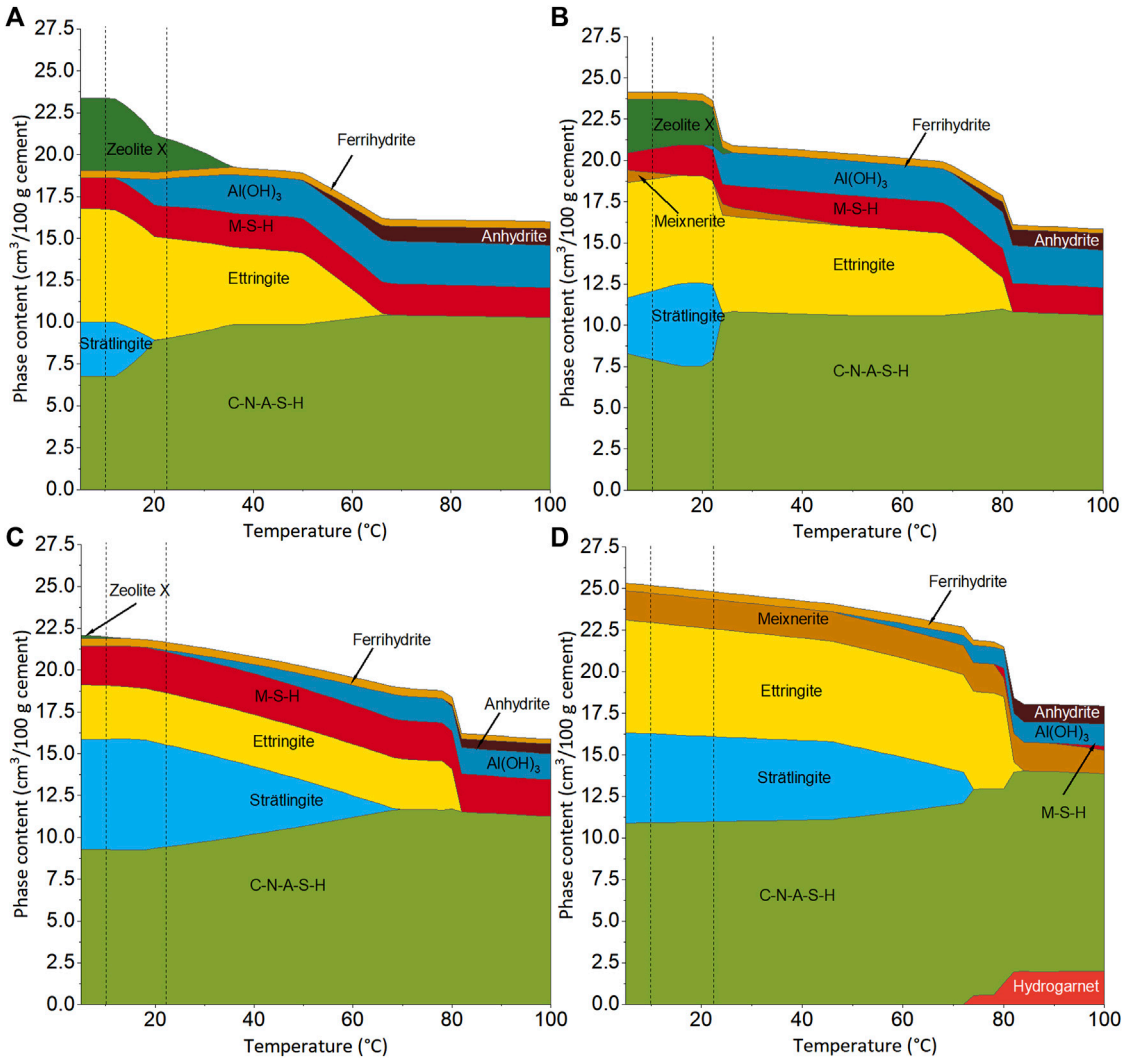

FIGURE 6
Modeled reaction products of the cement pastes C0S4 **(A)**, C5S4 **(B)**, C5S2 **(C)** and C14S4 **(D)** as a function of the curing temperature in absence of CO_2. Dotted lines mark 10 and 21.5°C.

4.3 Thermodynamic modeling

Figure 6 shows the modeled phase assemblages of the hybrid cements as a function of the curing temperature between 5 and 100°C in absence of CO_2. The introduction of CO_2 results in the formation of calcite but does not further alter the phase assemblage significantly (Supplementary Figure S6). In the relevant temperature range (10–21.5°C), the modeled hydration products are C-N-A-S-H, ettringite, strätlingite, meixnerite, M-S-H, $Al(OH)_3$, ferrihydrite and zeolite X (N-A-S-H gel). The formation of ettringite is expected as a result of the high sulfate content, introduced by the activator. This phase and C-N-A-S-H were observed in all cement pastes by XRD (Figure 3, Supplementary Figures S2–S5). A significant amount of meixnerite was modeled only for C14S4, again in line with the XRD results.

No portlandite was modeled for C14S4, although it was found with XRD and TGA/DTG in this paste. This can be assigned either to a higher amount of available Ca in the cement pastes than what followed from the DoHs assumed for the thermodynamic modeling, or to kinetic effects, *i.e.*, a slow consumption of portlandite through the pozzolanic reaction with GGBFS and FA. The latter appears more likely, as the amount of portlandite in the paste was found to be higher at 10°C than at 21.5°C (Figure 3).

N-A-S-H gel (modeled as zeolite X), $Al(OH)_3$ in cement pastes and ferrihydrite are generally of poor crystallinity and are, thus, often not detectable by XRD. The formation of M-S-H was

TABLE 4 Modeled reaction products (in cm^3/100 g cement) of the cement pastes C0S4, C5S4, C5S2 and C14S4 at curing temperatures of 10 and 21.5°C.

	C0S4		C5S4		C5S2		C14S4	
	10°C	21.5°C	10°C	21.5°C	10°C	21.5°C	10°C	21.5°C
C-N-A-S-H	6.8	9.0	7.9	7.9	9.3	9.4	10.9	11.0
Strätlingite	3.2	-	4.2	4.6	6.6	6.1	5.4	5.1
Ettringite	6.7	6.0	6.8	6.3	3.2	3.1	6.7	6.5
M-S-H	1.9	1.9	1.4	1.9	2.4	2.5	-	-
Meixnerite	-	-	0.4	-	-	-	1.8	1.8
$Al(OH)_3$	-	1.6	-	0.3	-	0.1	-	-
Zeolite X	4.3	2.0	3.0	2.3	0.1	-	-	-
Total volume	22.9	20.5	23.7	23.3	21.6	21.2	24.8	24.4

computed for C0S4, C5S4 and C5S2, *i.e.*, for the cements with no or a low amount of Pc. M-S-H is also poorly crystalline and therefore cannot be easily identified by XRD. However, its formation is generally slow (Brew and Glasser, 2005; Bernard et al., 2019); thus, it cannot be conclusively decided whether this phase was present in the cement pastes or not.

The fact that strätlingite was modeled as a major hydration product in all cement pastes (except C0S4 cured at 21.5°C; see discussion below) strongly suggests that the AFm phase found by ^{27}Al MAS NMR and indicated by the TGA/DTG results for all cements was strätlingite. Its occurrence is expected in systems with a high alumina availability such as the present cements, as has been previously shown by thermodynamic modeling of alkali-activated slags and OPC-SCM blends (Damidot and Glasser, 1995; Lothenbach et al., 2011; Myers et al., 2017). The failure to detect it by XRD in the present study is attributed to the fact that strätlingite is generally of poor crystallinity and thus gives only broad reflections in XRD patterns (e.g., Matschei et al., 2007a; Ke et al., 2017).

Thermodynamic modeling yields a significant change in the phase assemblage and total phase volume in the range approximately 12–35°C for C0S4 (Figure 6A) and around 22°C for C5S4 (Figure 6B). With increasing temperature, the amounts of zeolite X (N-A-S-H gel) and strätlingite decrease in both cements, while the amounts of $Al(OH)_3$ and C-N-A-S-H increase. These changes occur gradually in C0S4, while the changes are more abrupt in C5S4. For the present samples it follows that curing at 10°C leads to a higher volume of hydration products than curing at 21.5°C, mainly caused by differing amounts of strätlingite and N-A-S-H gel (Figure 6; Table 4). The computed increase of the volume of hydration products with decreasing curing temperature provides an explanation for the observed dependence of the compressive strength of C5S4 on curing temperature (Figure 2), because the compressive strength of cement pastes depends essentially only on their porosity, which is inversely related to the volume of hydration products (Rößler and Odler, 1985; Odler 1991; Lothenbach et al., 2008; Mota et al., 2018; Mota et al., 2019). The actual dependence of phase assemblage on temperature, including the phase assemblages at 10 and 21.5°C, may differ slightly from the computed assemblages due to slight inaccuracies and kinetic effects. This may be the reason for the fact that an AFm phase was detected in C0S4 cured at 21.5°C, but strätlingite was modeled only for lower temperatures for this cement paste.

Thermodynamic modeling indicated that also for the alkali-activated GGBFS/FA blend without Pc (C0S4), the total volume of hydration products is higher for curing at 10 °C than for curing at 21.5°C, caused by a higher volume of strätlingite and N-A-S-H gel. However, this prediction was not confirmed by the compressive strengths of C0S4, which were higher for curing at 21.5°C than for curing at 10°C for both curing times (28 and 91 days). This discrepancy is likely related to the assumptions regarding the DoHs of the starting materials: while these obviously provide a good estimate of the DoHs in the hybrid cements (see also below), they seem not to be applicable to cement C0S4, at least up to a curing time of 91 days. This is particularly relevant for the formation of N-A-S-H gel, as this depends strongly on the relative availability of Na, Ca, Al and Si in the system, and thus on the DoHs of the FA and the GGBFS. Therefore, the computed amounts of N-A-S-H (modeled as zeolite X) in C0S4 and C5S4 are best understood as indications of their occurrence, and they may only reflect an advanced stage of the hydration of these cements.

For the other two cement pastes, C5S2 (Figure 6C) and C14S4 (Figure 6D), the same phases were computed for the complete relevant temperature range (except a minor amount of $Al(OH)_3$ for C5S2 at 21.5°C); however, also for these pastes the modeled total volume of hydration products decreased from 10 to 21.5°C. As above for C5S4, this explains the observed dependence of the compressive strengths of the hybrid cements on the curing temperature. The decrease of volume of hydration products is mainly due to a decrease of the amount of strätlingite, which is not

fully compensated by the corresponding increase of the volume of C-N-A-S-H (Figure 6; Table 4). Again, while the absolute amounts of hydration products may not be fully accurate, it is evident that there is a trend of increasing volume of hydration products with decreasing curing temperature for these two cement pastes, in agreement with the ^{27}Al MAS NMR and TGA/DTG results.

The above conclusions drawn from the modeling results remain valid for moderate variations of the degrees of hydration (DoHs) of the Portland clinker and the GGBFS. Setting the DoH of the Pc in the Portland clinker-containing hybrid cements to 60% or 80% did not change the modeled phase assemblage of the hydrated cements at curing temperatures of 10 and 21.5°C, compared to the cements with a DoH of the Pc of 70%, and the phase abundances were comparable for all three DoHs (Supplementary Figures S7, S8). Likewise, the phase assemblages of the cements with a DoH of the GGBFS of either 50% or 70% were similar to those of the cements with a DoH of the GGBFS of 60%, except that a minor amount of meixnerite was modeled for C0S4 and C5S2 at 10 °C when the DoH of the GGBFS was set to 70% (Supplementary Figures S9, S10).

More significant differences exist between the modeled phase assemblages of the cements with the DoH of the fly ash being 10%, 20 and 30%, respectively. For a DoH of the fly ash of 10%, no M-S-H and no $Al(OH)_3$ were modeled in the relevant temperature range 10–21.5°C (except a minor amount of M-S-H in C0S4), the amounts of strätlingite were considerably lower for all cements, and the formation of hydrogarnet was modeled for C14S4 for both curing temperatures (Supplementary Figure S11). The phase assemblages modeled for a DoH of the fly ash of 30% differ from that modeled for a DoH of 20% *inter alia* in that no or only low amounts of strätlingite are present in C0S4 and C5S2, that $Al(OH)_3$ is found in higher amounts and/or over a greater temperature range for all cements, and that a significant amount of zeolite X (N-A-S-H) is found in C14S4 (Supplementary Figure S12). It is thus evident that the DoH of the fly ash has a particularly strong effect on the equilibrium phase assemblage of the hybrid cements and the alkali-activated GGBFS/FA blend. Nevertheless, the essential conclusions drawn above remain valid also for variations of the DoH of the fly ash, because for all DoHs modeling yields a decrease of the volume of hydration products with increasing curing temperature for all cements, and strätlingite was predicted to form for DoHs of 10% as well as 30% for most of the cements (Supplementary Figures S11, S12). In addition, it is noted that the fact that the formation of hydrogarnet was predicted for a DoH of the fly ash of 10% for C14S4 (Supplementary Figure S11), while this phase was not identified by XRD, may be taken as an indication that the actual DoH of the fly ash in the cement pastes was higher than 10%.

5 Conclusion

For the three hybrid cements containing Portland clinker (C5S4, C5S2 and C14S4), the results obtained with ^{27}Al MAS NMR, TGA/DTA and thermodynamic modeling were in reasonable agreement. The results show that in these cements, a higher volume of hydration products is formed at 10°C, compared to curing at 21.5°C, mainly due to the formation of strätlingite at the expense of C-N-A-S-H. This explains the observed dependence of compressive strength on curing temperature, because the compressive strength of a cement paste depends on the volume of hydration products (Rößler and Odler, 1985; Odler 1991; Lothenbach et al., 2008; Mota et al., 2018; Mota et al., 2019). The thermodynamic modeling as applied here pertains to the equilibrium state of the cement pastes, *i.e.*, to the state when the assumed final degrees of hydration (DoH) have been reached by all starting materials; this state is more closely approached after 91 days of curing than after 28 days of curing.

For the alkali-activated GGBFS/FA blend (C0S4), a higher volume of hydration products was also modeled for curing at 10°C, compared to curing at 21.5°C. However, this was not reflected in the measured compressive strengths; *i.e.*, the strengths of this cement were higher for curing at 21.5°C. The fact that the difference between the compressive strengths decreased with curing time indicates that the final DoHs to which the modeling results pertain had not reached after 91 days of curing. The discrepancy between the modeling results and the observed compressive strengths is possibly also related to difficulties to accurately model the abundance of N-A-S-H gel, which is expected to be a particularly important cementitious phase in C0S4.

The fact that strätlingite could not be detected in the cement pastes by XRD, while the formation of strätlingite was predicted by thermodynamic modeling and an AFm or LDH phase was evidenced by the ^{27}Al MAS NMR and TGA/DTG results, is explained by the generally low crystallinity of strätlingite, resulting in very broad reflections in XRD patterns (Matschei et al., 2007a; Ke et al., 2017).

The present findings demonstrate that analytical results and engineering properties measured on hybrid cements and materials derived from them, cured and stored at usual laboratory temperatures (20–25°C), are not fully transferable to lower temperatures. This is relevant *inter alia* in contexts where hybrid cements are applied for sub-surface structures, for example sealing structures in underground waste storage facilities when the expected curing and service conditions involve significantly lower temperatures, or when the temperature oscillates.

Data availability statement

The raw data supporting the conclusion of this article will be made available by the authors, without undue reservation.

Author contributions

RH: formal analysis, investigation, writing—original draft, visualization; PS: conceptualization, methodology, formal analysis, writing—review and editing, supervision, project administration, funding acquisition; DAG: investigation; SK: writing—review and editing, supervision; BW: formal analysis, writing—review and editing, visualization; GJGG: conceptualization, methodology, writing—original draft, writing—review and editing, supervision.

Funding

This study was supported by internal funds within the framework of BAM's MI programme (project MIT1-2019-34).

Acknowledgments

The authors thank Nico Vogler (BAM) for carrying out the thermogravimetric analyses.

Conflict of interest

The authors declare that the research was conducted in the absence of any commercial or financial relationships that could be construed as a potential conflict of interest.

Publisher's note

All claims expressed in this article are solely those of the authors and do not necessarily represent those of their affiliated organizations, or those of the publisher, the editors and the reviewers. Any product that may be evaluated in this article, or claim that may be made by its manufacturer, is not guaranteed or endorsed by the publisher.

Supplementary material

The Supplementary Material for this article can be found online at: https://www.frontiersin.org/articles/10.3389/fmats.2022.982568/full#supplementary-material

References

Alahrache, S., Winnefeld, F., Champenois, J.-B., Hesselbarth, F., and Lothenbach, B. (2017). Chemical activation of hybrid binders based on siliceous fly ash and Portland cement. *Cem. Concr. Compos.* 66, 10–23. doi:10.1016/j.cemconcomp.2015.11.003

Andersen, M. D., Jakobsen, H. J., and Skibsted, J. (2004). Characterization of white Portland cement hydration and the C-S-H structure in the presence of sodium aluminate by ^{27}Al and ^{29}Si MAS-NMR spectroscopy. *Cem. Concr. Res.* 34, 857–868. doi:10.1016/j.cemconres.2003.10.009

Angulo-Ramírez, D. E., Mejía de Gutiérrez, R., and Puertas, F. (2017). Alkali-activated Portland blast-furnace slag cement: mechanical properties and hydration. *Constr. Build. Mater.* 140, 119–128. doi:10.1016/j.conbuildmat.2017.02.092

Bach, T. T. H., Cau Dit Coumes, C., Pochard, I., Mercier, C., Revel, B., and Nonat, A. (2012). Influence of temperature on the hydration products of low pH cements. *Cem. Concr. Res.* 42, 805–817. doi:10.1016/j.cemconres.2012.03.009

Bahafid, S., Ghabezloo, S., Duc, M., Faure, P., and Sulem, J. (2017). Effect of the hydration temperature on the microstructure of class G cement: C-S-H composition and density. *Cem. Concr. Res.* 95, 270–281. doi:10.1016/j.cemconres.2017.02.008

Ben Haha, M., Lothenbach, B., Le Saout, G., and Winnefeld, F. (2012). Influence of slag chemistry on the hydration of alkali-activated blast-furnace slag — Part II: Effect of Al2O3. *Cem. Concr. Res.* 42, 74–83. doi:10.1016/j.cemconres.2011.08.005

Bernal, S. A., Provis, J. L., Walkley, B., San Nicolas, R., Gehman, J. D., Brie, D. G., et al. (2013). Gel nanostructure in alkali-activated binders based on slag and fly ash, and effects of accelerated carbonation. *Cem. Concr. Res.* 53, 127–144. doi:10.1016/j.cemconres.2013.06.007

Bernal, S. A., San Nicolas, R., Myers, R. J., Mejia de Gutierrez, R., Puertas, F., van Deventer, J. S. J., et al. (2014). MgO content of slag controls phase evolution and structural changes induced by accelerated carbonation in alkali-activated binders. *Cem. Concr. Res.* 57, 33–43. doi:10.1016/j.cemconres.2013.12.003

Bernard, E., Lothenbach, B., Chlique, C., Wyrzykowski, M., Dauzeres, A., Pochard, I., et al. (2019). Characterization of magnesium silicate hydrate (M-S-H). *Cem. Concr. Res.* 116, 309–330. doi:10.1016/j.cemconres.2018.09.007

Brew, D. R. M., and Glasser, F. P. (2005). Synthesis and characterisation of magnesium silicate hydrate gels. *Cem. Concr. Res.* 35, 85–98. doi:10.1016/j.cemconres.2004.06.022

Burciaga-Diaz, O., and Escalante-Garcia, J. I. (2013). Structure, mechanisms of reaction, and strength of an alkali-activated blast-furnace slag. *J. Am. Ceram. Soc.* 96, 3939–3948. doi:10.1111/jace.12620

Dai, Z., Tran, T. T., and Skibsted, J. (2014). Aluminium incorporation in the C-S-H phase of white Portland cement-metakaolin blends studied by ^{27}Al and ^{29}Si MAS NMR spectroscopy. *J. Am. Ceram. Soc.* 97, 2662–2671. doi:10.1111/jace.13006

Damidot, D., and Glasser, F. P. (1995). Investigation of the CaO-Al_2O_3-SiO_2-H_2O system at 25°C by thermodynamic calculations. *Cem. Concr. Res.* 25, 22–28. doi:10.1016/0008-8846(94)00108-B

De Weerdt, K., Ben Haha, M., Le Saout, G., Kjellsen, K. O., Justnes, H., and Lothenbach, B. (2011). Hydration mechanisms of ternary Portland cements containing limestone powder and fly ash. *Cem. Concr. Res.* 41, 279–291. doi:10.1016/j.cemconres.2010.11.014

Donatello, S., Fernandez-Jimenez, A., and Palomo, A. (2018). Very high volume fly ash cements. Early age hydration study using Na_2SO_4 as an activator. *J. Am. Ceram. Soc.* 96, 900–906. doi:10.1111/jace.12178

Escalante-Garcia, J. I. (2003). Nonevaporable water from neat OPC and replacement materials in composite cements hydrated at different temperatures. *Cem. Concr. Res.* 33, 1883–1888. doi:10.1016/S0008-8846(03)00208-4

Escalante-Garcia, J. I., and Sharp, J. H. (1998). Effect of temperature on the hydration of the main clinker phases in Portland cements: Part II, blended cements. *Cem. Concr. Res.* 28, 1259–1274. doi:10.1016/S0008-8846(98)00107-0

Eysel, W., Höfer, H. H., Keester, K. L., and Hahn, T. (1985). Crystal chemistry and structure of Na_2SO_4 I and its solid solutions. *Acta Crystallogr. B* 41, 5–11. doi:10.1107/S0108768185001501

Frias, M., and Martinez-Ramirez, S. (2014). Use of micro-Raman spectroscopy to study reaction kinetics in blended white cement pastes containing metakaolin. *J. Raman Spectrosc.* 40, 2063–2068. doi:10.1002/JRS.2372

Fu, J., Bligh, M. W., Shikhov, I., Jones, A. M., Holt, C., Keyte, L. M., et al. (2021). A microstructural investigation of a Na_2SO_4 activated cement-slag blend. *Cem. Concr. Res.* 150, 106609. doi:10.1016/j.cemconres.2021.106609

Garcia-Lodeiro, I., Donatello, S., Fernández-Jiménez, A., and Palomo, A. (2016). Hydration of hybrid alkaline cement containing a very large proportion of fly ash: a descriptive model. *Materials* 9, 605. doi:10.3390/ma9070605

Garcia-Lodeiro, I., Fernandez-Jimenez, A., and Palomo, A. (2013). Hydration kinetics in hybrid binders: early reaction stages. *Cem. Concr. Compos.* 39, 82–92. doi:10.1016/j.cemconcomp.2013.03.025

Gardner, L. J., Bernal, S. A., Wailing, S. A., Corkhill, C. L., Provis, J. L., and Hyatt, N. C. (2015). Characterisation of magnesium potassium phosphate cements

blended with fly ash and ground granulate blast furnace slag. *Cem. Concr. Res.* 74, 76–87. doi:10.1016/j.cemconres.2015.01.015

Gluth, G. J. G., and Garel, S. (2021). "Calorimetry study of the influence of Portland cement content, slag/fly ash ratio, and activator type on the early hydration of hybrid cements," in *Proceedings of the 3rd RILEM spring convention and conference (RSCC 2020) – volume 2: New materials and structures for ultra-durability*. Editors I. B. Valente, A. Ventura Gouveia, and S. S. Dias (Cham: Springer), 217–226. doi:10.1007/978-3-030-76551-4_20

Gluth, G. J. G., Lehmann, C., Rübner, K., and Kühne, H.-C. (2014). Reaction products and strength development of wastepaper sludge ash and the influence of alkalis. *Cem. Concr. Compos.* 45, 82–88. doi:10.1016/j.cemconcomp.2013.09.009

Gomez-Zamorano, L., Balonis, M., Erdemli, B., Neithalath, N., and Sant, G. (2017). C-(N)-S-H and N-A-S-H gels: compositions and solubility data at 25°C and 50 °C. *J. Am. Ceram. Soc.* 100, 2700–2711. doi:10.1111/jace.14715

He, H., Guo, J., Zhu, J., Yuan, P., and Hu, C. (2004). ^{29}Si and ^{27}Al MAS NMR spectra of mullites from different kaolinites. *Spectrochimica Acta Part A Mol. Biomol. Spectrosc.* 60, 1061–1064. doi:10.1016/S1386-1425(03)00337-8

Helgeson, H. C., Kirham, D. H., and Flowers, G. C. (1981). Theoretical prediction of the thermodynamic behavior of aqueous electrolytes at high pressures and temperatures: IV. Calculation of activity coefficients, osmotic coefficients, and apparent molal and standard and relative partial molal properties to 600 °C and 5 kb. *Am. J. Sci.* 281, 1249–1516. doi:10.2475/ajs.281.10.1249

Hu, Z., Wyrzykowski, M., and Lura, P. (2020). Estimation of reaction kinetics of geopolymers at early ages. *Cem. Concr. Res.* 129, 105971. doi:10.1016/j.cemconres.2020.105971

Jackson, M. D., Chae, S. R., Mulcahy, S. R., Meral, C., Taylor, R., Li, P., et al. (2013). Unlocking the secrets of Al-tobermorite in Roman seawater concrete. *Am. Mineral.* 98, 1669–1687. doi:10.2138/am.2013.4484

Jackson, M. D., Landis, E. N., Brune, P. F., Vitti, M., Chen, H., Li, Q., et al. (2014). Mechanical resilience and cementitious processes in imperial Roman architectural mortar. *Proc. Natl. Acad. Sci. U. S. A.* 111, 18484–18489. doi:10.1073/pnas.1417456111

Jackson, M. D., Oleson, J. P., Moon, J., Zhang, Y., Chen, H., and Gudmundsson, M. T. (2018). Extreme durability in ancient roman concretes. *Am. Ceram. Soc. Bull.* 97 (5), 22–28.

Jones, M. R., Macphee, D. E., Chudek, J. A., Hunter, G., Lannegrand, R., Talero, R., et al. (2003). Studies using ^{27}Al MAS NMR of AFm and AFt phases and the formation of Friedel´s salt. *Cem. Concr. Res.* 33, 177–182. doi:10.1016/S0008-8846(02)00901-8

Joseph, S., Skibsted, J., and Cizer, Ö. (2020). Hydration of polyphase Ca_3SiO_5-$Ca_3Al_2O_6$ in the presence of gypsum and Na2SO4. *J. Am. Ceram. Soc.* 103, 6461–6474. doi:10.1111/jace.17321

Ke, X., Bernal, S. A., and Provis, J. L. (2017). Uptake of chloride and carbonate by Mg-Al and Ca-Al layered double hydroxides in simulated pore solutions of alkali-activated slag cement. *Cem. Concr. Res.* 100, 1–13. doi:10.1016/j.cemconres.2017.05.015

Kulik, D. A., Wagner, T., Dmytrieva, S. V., Kosakowski, G., Hingerl, F. F., Chudnenko, K. V., et al. (2013). GEM-Selektor geochemical modeling package: revised algorithm and GEMS3K numerical kernel for coupled simulation codes. *Comput. Geosci.* 17, 1–24. doi:10.1007/s10596-012-9310-6

Kunhi Mohammed, A., Moutzouri, P., Berruyer, P., Walder, B. J., Siramanont, J., Harris, M., et al. (2020). The atomic-level structure of cementitious calcium aluminate silicate hydrate. *J. Am. Chem. Soc.* 142, 11060–11071. doi:10.1021/jacs.0c02988

Kwan, S., LaRosa, J., and Grutzeck, M. W. (1995). ^{29}Si and ^{27}Al MAS NMR study of strätlingite. *J. Am. Ceram. Soc.* 78, 1921–1926. doi:10.1111/J.1151-2916.1995.TB08910.X

Lee, C. Y., Lee, H. K., and Lee, K. M. (2003). Strength and microstructural characteristics of chemically activated fly ash-cement systems. *Cem. Concr. Res.* 33, 425–431. doi:10.1016/S0008-8846(02)00973-0

Lothenbach, B., Durdziński, P., and De Weerdt, K. (2016). "Thermogravimetric analysis," in *A practical guide to microstructural analysis of cementitious materials*. Editors K. Scrivener, R. Snellings, and B. Lothenbach (Boca Raton: CRC Press), 177–211.

Lothenbach, B., Kulik, D. A., Matschei, T., Balonis, M., Baquerizo, L., Dilnesa, B., et al. (2019). Cemdata18: a chemical thermodynamic database for hydrated Portland cements and alkali-activated materials. *Cem. Concr. Res.* 115, 472–506. doi:10.1016/j.cemconres.2018.04.018

Lothenbach, B., Matschei, T., Möschner, G., and Glasser, F. P. (2008). Thermodynamic modelling of the effect of temperature on the hydration and porosity of Portland cement. *Cem. Concr. Res.* 38, 1–18. doi:10.1016/j.cemconres.2007.08.017

Lothenbach, B., Pelletier-Chaignat, L., and Winnefeld, F. (2012). Stability in the system $CaO–Al_2O_3–H_2O$. *Cem. Concr. Res.* 42, 1621–1634. doi:10.1016/j.cemconres.2012.09.002

Lothenbach, B., Scrivener, K., and Hooton, R. D. (2011). Supplementary cementitious materials. *Cem. Concr. Res.* 41, 1244–1256. doi:10.1016/j.cemconres.2010.12.001

Lothenbach, B., Winnefeld, F., Alder, C., Wieland, E., and Lunk, P. (2007). Effect of temperature on the pore solution, microstructure and hydration products of Portland cement pastes. *Cem. Concr. Res.* 37, 483–491. doi:10.1016/j.cemconres.2006.11.016

Matschei, T., Lothenbach, B., and Glasser, F. P. (2007b). The AFm phase in Portland cement. *Cem. Concr. Res.* 37, 118–130. doi:10.1016/j.cemconres.2006.10.010

Matschei, T., Lothenbach, B., and Glasser, F. P. (2007a). Thermodynamic properties of Portland cement hydrates in the system $CaO-Al_2O_3-SiO_2-CaSO_4-CaCO_3-H_2O$. *Cem. Concr. Res.* 37, 1379–1410. doi:10.1016/j.cemconres.2007.06.002

Mota, B., Matschei, T., and Scrivener, K. (2018). Impact of NaOH and Na_2SO_4 on the kinetics and microstructural development of white cement hydration. *Cem. Concr. Res.* 108, 172–185. doi:10.1016/j.cemconres.2018.03.017

Mota, B., Matschei, T., and Scrivener, K. (2019). Impact of sodium gluconate on white cement-slag systems with Na_2SO_4. *Cem. Concr. Res.* 122, 59–71. doi:10.1016/j.cemconres.2019.04.008

Murgier, S., Zanni, H., and Gouvenot, D. (2014). Blast furnace slag cement: a ^{29}Si and ^{27}Al NMR study. *C. R. Chim.* 7, 389–394. doi:10.1016/J.CRCI.2004.02.004

Myers, R. J., Bernal, S. A., and Provis, J. L. (2014). A thermodynamic model for C-(N-)A-S-H gel: CNASH_ss. Derivation and validation. *Cem. Concr. Res.* 66, 27–47. doi:10.1016/j.cemconres.2014.07.005

Myers, R. J., Bernal, S. A., and Provis, J. L. (2017). Phase diagrams for alkali-activated slag binders. *Cem. Concr. Res.* 95, 30–38. doi:10.1016/j.cemconres.2017.02.006

Myers, R. J., Bernal, S. A., San Nicolas, R., and Provis, J. L. (2013). Generalized structural description of calcium-sodium aluminosilicate hydrate gels: the cross-linked substituted tobermorite model. *Langmuir* 29, 5294–5306. doi:10.1021/la4000473

Myers, R. J., Lothenbach, B., Bernal, S. A., and Provis, J. L. (2015). Thermodynamic modelling of alkali-activated slag cements. *Appl. Geochem.* 61, 233–247. doi:10.1016/J.APGEOCHEM.2015.06.006

Odler, I. (1991). Strength of cement (final report). *Mater. Struct.* 24, 143–157. doi:10.1007/BF02472476

Palomo, A., Monteiro, P., Martauz, P., Bilek, V., and Fernandez-Jimenez, A. (2019). Hybrid binders: a journey from the past to a sustainable future (*opus caementicium futurum*). *Cem. Concr. Res.* 14, 105829. doi:10.1016/j.cemconres.2019.105829

Parrot, L. J., and Killoh, D. C. (1984). Prediciton of cement hydration. *Br. Ceram. Proc.* 35, 41–53.

Renaudin, G., Russias, J., Leroux, F., Cau-dit-Coumes, C., and Frizon, F. (2009). Structural characterization of C-S-H and C-A-S-H samples—Part II: Local environment investigated by spectroscopic analyses. *J. Solid State Chem.* 182, 3320–3329. doi:10.1016/J.JSSC.2009.09.024

Rößler, M., and Odler, I. (1985). Investigations on the relationship between porosity, structure and strength of hydrated Portland cement pastes I. Effect of porosity. *Cem. Concr. Res.* 15, 320–330. doi:10.1016/0008-8846(85)90044-4

Sanz, J., Madani, A., Serratosa, J. M., Moya, J. S., and Aza, S. (1984). Aluminum-27 and silicon-29 magic-angle spinning nuclear magnetic resonance study of the kaolinite-mullite transformation. *J. Am. Ceram. Soc.* 71, 418–421. doi:10.1111/j.1151-2916.1988.tb07513.x

Shi, C., Fernández-Jiménez, A., and Palomo, A. (2011). New cements for the 21st century: the pursuit of an alternative to Portland cement. *Cem. Concr. Res.* 41, 750–763. doi:10.1016/j.cemconres.2011.03.016

Skibsted, J., Henderson, E., and Jakobsen, H. J. (1993). Characterization of calcium aluminate phases in cements by ^{27}Al MAS NMR spectroscopy. *Inorg. Chem.* 32, 1013–1027. doi:10.1021/ic00058a043

Snellings, R., Bazzoni, A., and Scrivener, K. (2014). The existence of amorphous phase in Portland cements: Physical factors affecting Rietveld quantitative phase analysis. *Cem. Concr. Res.* 59, 139–146. doi:10.1016/j.cemconres.2014.03.002

Sun, G. K., Young, J. F., and Kirkpatrick, R. J. (2006). The role of Al in C-S-H: NMR, XRD, and compositional results for precipitated samples. *Cem. Concr. Res.* 36, 18–29. doi:10.1016/j.cemconres.2005.03.002

Sun, Z., and Vollpracht, A. (2018). Isothermal calorimetry and *in-situ* XRD study of the NaOH activated fly ash, metakaolin and slag. *Cem. Concr. Res.* 103, 110–122. doi:10.1016/j.cemconres.2017.10.004

Taylor, H. F. W. (1987). A method for predicting alkazi ion concentrations in cement pore solutions. *Adv. Cem. Res.* 1, 5–17. doi:10.1680/adcr.1987.1.1.5

Taylor, H. F. W., Famy, C., and Scrivener, K. L. (2001). Delayed ettringite formation. *Cem. Concr. Res.* 31, 683–693. doi:10.1016/S0008-8846(01)00466-5

Thiery, M., Villain, G., Dangla, P., and Platret, G. (2007). Investigation of the carbonation front shape on cementitious materials: effects of the chemical kinetics. *Cem. Concr. Res.* 37, 1047–1058. doi:10.1016/j.cemconres.2007.04.002

Wagner, T., Kulik, D. A., Hingerl, F. F., and Dmytrieva, S. V. (2012). GEM-Selektor geochemical modeling package: TSolMod library and data interface for multicomponent phase models. *Can. Mineralogist* 50, 1173–1195. doi:10.3749/canmin.50.5.1173

Walkley, B., Ke, X., Hussein, O. H., Bernal, S. A., and Provis, J. L. (2020). "Thermodynamic properties of (N,K)-A-S-H gels," in *74th RILEM annual week & 40th cement and concrete science conference*. Editors D. Geddes, S. Ghazizadeh, S. Kearney, G. Koma, C. Le Gaillard, and J. L. Provis. Sheffield. Article No. 104.

Walkley, B., and Provis, J. L. (2019). Solid-state nuclear magnetic resonance spectroscopy of cements. *Mater. Today Adv.* 1, 100007. doi:10.1016/J.MTADV.2019.100007

Wiedemann, H. G., and Smykatz-Kloss, W. (1981). Thermal studies on thenardite. *Thermochim. Acta* 50, 17–29. doi:10.1016/0040-6031(81)85039-3

Xue, L., Zhang, Z., and Wang, H. (2021). Early hydration kinetics and microstructure development of hybrid alkali activated cements (HAACs) at room temperature. *Cem. Concr. Compos.* 123, 104200. doi:10.1016/j.cemconcomp.2021.104200